JOURNAL OF PROPULSION AND POWER
Vol. 25, No. 3, May–June 2009

Development and Application of an Arbitrary Lagrangian Eulerian Solver for Turbomachinery Aeromechanics

Kishore Ramakrishnan,[*] Dana A. Gottfried,[†] Patrick B. Lawless,[‡] and Sanford Fleeter[§]
Purdue University, West Lafayette, Indiana 47907

DOI: 10.2514/1.36068

This paper describes the development and application of turbomachinery aeromechanics arbitrary Lagrangian Eulerian 3-D, an arbitrary Lagrangian Eulerian finite-element-coupled fluid–structure interaction solver, to axial and radial flow turbomachinery aeromechanics issues. The incorporation of turbomachinery-specific algorithms enables the analysis of crack generation in the inlet guide vanes of a modern transonic compressor due to resonant vibrations generated by the potential/shock field of the downstream rotor. The capability to model turbulent wake forcing functions makes possible predictions of the resonant vibratory stress resulting from the subsonic rotor wakes interacting with the downstream stators. The modification of outflow boundary conditions to model incoming acoustic waves allows the unsteady aerodynamic response of a high-speed centrifugal compressor impeller to the potential field/shock excitation generated by the downstream radial-vaned diffuser to be simulated. Finally, the impeller blade aerodynamic damping is calculated to quantify the effect of blade-motion-induced aerodynamics at the exducer. The results make a case that, with increasing computing capacity, coupled fluid–structure interaction methods can become the approach of choice for high cycle fatigue design predictions.

Nomenclature

b = body force vector
D_{ij} = deformation rate tensor
E = specific internal energy
G = shear modulus
K = bulk modulus
n = unit normal pointing out of control surface
P = isotropic part of stress tensor
P_t = thermodynamic pressure
P_m = mechanical pressure
q = shock smearing factor
S = element surface
S_{ij} = deviatoric stress tensor
T = temperature/time period
U = mesh velocity
$\cancel{V}$ = element volume
u = material velocity
$u_{i,j}$ = velocity gradient tensor
γ = ratio of specific heats
ε_{ij} = strain tensor
κ = thermal conductivity
μ = (total) dynamic viscosity
σ_{ij} = stress tensor
ω = angular frequency/vorticity

I. Introduction

BLADE failure due to high cycle fatigue (HCF) is a critical concern throughout the gas turbine industry, with HCF analysis a key technology development issue. HCF arises due to the flow-induced vibratory response of turbomachinery blading. Whereas computational fluid dynamic tools to model turbomachinery unsteady aerodynamics and structural dynamic solvers to model the blade vibratory response have evolved independently, HCF is a coupled problem in which the unsteady aerodynamics affects the blade motion and vice versa. This requires the unsteady aerodynamics and structural dynamics to be dealt with simultaneously. Toward this end, capabilities to simulate the vibratory motion have been added/interfaced to unsteady Euler/Navier–Stokes solvers to calculate blade vibrations [1–3]. However, the data transfer between the fluid and structural grids is time consuming and can limit the accuracy of the aeroelastic simulation [4].

A coupled fluid–structure analysis alleviates these limitations while minimizing interpolation errors due to the data transfer. By predicting the unsteady aerodynamics and the vibratory stresses in a single simulation, it reduces the number of steps in the HCF analysis process (Fig. 1). Because the same finite element model is used to discretize the equations for the fluid and the structure, it obviates the need for data transfer algorithms. Thus, it better captures the inherently nonlinear coupling between the fluid and the structure, allowing more accurate predictions of the vibratory stresses responsible for HCF.

Turbomachinery aeromechanics arbitrary Lagrangian Eulerian 3-D (TAM-ALE3D) is a 3-D finite element solver with multimaterial capability. The arbitrary Lagrangian Eulerian (ALE) solver makes it suitable for the simulation of the fluid–structure interaction between the airfoil and the flow exciting it. The ALE formulation treats the fluid–structure problem as one system, with the model formulated such that the governing equations are discretized in a unified fashion and integrated simultaneously in time. This approach, combining the best features of both Lagrangian and Eulerian methods, was first introduced by Hirt et al. [5] for fluid flows at all speeds. Since then, it has come to be used widely for transient, high-speed, large deformation problems of solids [6]. Donea [7] used the ALE formulation to model fluid–structure interaction because the freedom of moving the mesh in this formulation was advantageous for treating relative sliding at the fluid–structure interface. Bendikson [8] used this approach for flutter calculations and demonstrated that it minimized errors in energy transfer between the fluid and the structure.

Presented as Paper 0627 at the 2006 Aerospace Sciences Conference, Reno, NV, 4–7 January 2006; received 5 December 2007; revision received 1 October 2008; accepted for publication 22 December 2008.

[*] Graduate Research Assistant, School of Mechanical Engineering; currently General Electric Global Research Center, Niskayuna, New York. Member AIAA.

[†] Post Doctoral Research Associate, School of Mechanical Engineering. Member AIAA.

[‡] Associate Professor, School of Mechanical Engineering; currently XcelAero Corporation, Houston, Texas. Associate Fellow AIAA.

[§] McAllister Distinguished Professor, School of Mechanical Engineering. Fellow AIAA.

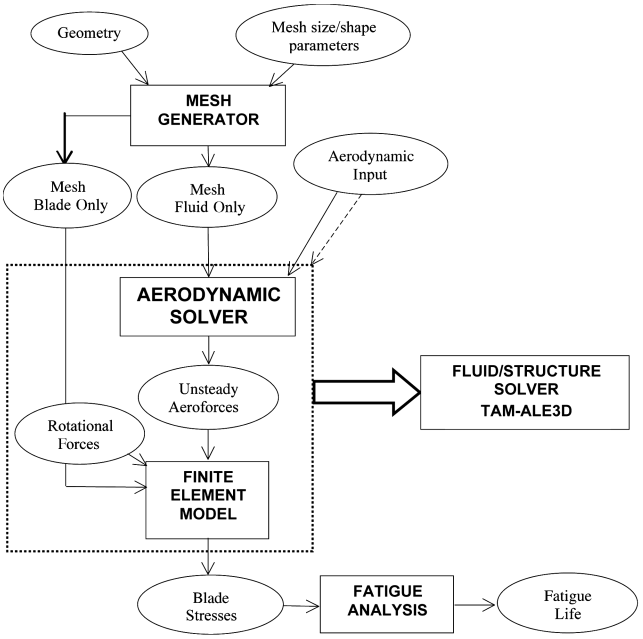

Fig. 1 HCF prediction systems.

By modeling the fluid and the structural domains using the same finite element method, the ALE formulation in TAM-ALE3D allows a seamless coupling between the two. Modeling and boundary-condition routines are added to enable application to a wide range of axial and radial flow turbomachinery aeromechanics problems. This paper describes these modeling additions and enhanced capabilities, with the solver used to analyze turbomachine aeromechanics issues.

The incorporation of turbomachinery-specific algorithms by Gottfried [9] enables the analysis of crack generation in the inlet guide vanes (IGVs) of a modern transonic compressor due to resonant vibrations generated by the potential/shock field of the downstream rotor. The incorporation of the capability to model turbulent wake forcing functions by Ramakrishnan [10] makes possible predictions of the resonant vibratory stress resulting from the subsonic rotor wakes interacting with the downstream stators. The modification of outflow boundary conditions to model incoming acoustic waves [11] allows the unsteady aerodynamic response of a high-speed centrifugal compressor impeller to the potential field/shock excitation generated by the downstream radial-vaned diffuser to be simulated. Lastly, the impeller blade aerodynamic damping is calculated to quantify the effect of blade-motion-induced aerodynamics at the exducer.

II. Mathematical Model

The mass, momentum, and energy equations are marched forward in time, with the physical domain discretized by an assembly of hexahedral elements. These elements are not required to move with the material as in a Lagrangian calculation nor remain fixed in space as in an Eulerian method. Rather, they are allowed to move independent of the continuum, making the scheme an arbitrary Lagrangian Eulerian scheme.

The governing equations are written with respect to a reference frame moving with an arbitrary velocity. The mass, momentum, and energy conservation equations for a control volume $\mathcal{V}$ of the continuum enclosed by the surface $S(x_i, t) = 0$ are

$$\frac{\partial}{\partial t}\int_{\mathcal{V}} \rho \, \mathrm{d}\mathcal{V} + \int_S \rho(u_i - U_i) n_i \, \mathrm{d}S = 0 \tag{1}$$

$$\frac{\partial}{\partial t}\int_{\mathcal{V}} \rho u_i \, \mathrm{d}\mathcal{V} + \int_S \rho u_i (u_i - U_i) n_i \, \mathrm{d}S = \int_S (n_j \sigma_{ij} - q n_i) \mathrm{d}S + \int_{\mathcal{V}} \rho b_i \, \mathrm{d}\mathcal{V} \tag{2}$$

$$\frac{\partial}{\partial t}\int_{\mathcal{V}} \rho E \, \mathrm{d}\mathcal{V} + \int_S \rho E (u_i - U_i) n_i \, \mathrm{d}S = \int_{\mathcal{V}} (\sigma_{ij} u_{i,j} - q u_{i,i}) \, \mathrm{d}\mathcal{V} + \int_{\mathcal{V}} \frac{\partial}{\partial x_i}\left(\kappa \frac{\partial T}{\partial x_i}\right) \mathrm{d}\mathcal{V} \tag{3}$$

where u_i denotes the material velocity, $U_i = \partial x_i / \partial t$ is the grid velocity, x_i is the position vector of any point on the surface of the control volume, $u_{i,j}$ is the velocity gradient tensor, σ_{ij} is the stress tensor (symmetric), and the q term is the shock viscosity which is used to smear shocks over a region comparable to the mesh spacing so that a very fine mesh is not needed in the vicinity of the shock.

The stress tensor is given by $\sigma_{ij} = -P\delta_{ij} + S_{ij}$ where P and S_{ij} represent the isotropic and deviatoric parts of stress tensor, respectively. For a Newtonian fluid, they are

$$P_t = (\gamma - 1)\rho E \tag{4}$$

$$S_{ij} = 2\mu\left(D_{ij} - \tfrac{1}{3} u_{i,i}\delta_{ij}\right) \tag{5}$$

whereas, for a linear elastic solid, we have

$$P_m = K \frac{\mathcal{V}_{\mathrm{ref}} - \mathcal{V}}{\mathcal{V}} \tag{6}$$

$$S_{ij} = 2G\left(\varepsilon_{ij} - \tfrac{1}{3}\varepsilon_{i,i}\delta_{ij}\right) \tag{7}$$

Note that the isotropic part of the stress tensor is interpreted as the thermodynamic pressure for the fluid and the mechanical pressure for the solid.

Equations (1–3) are solved by an operator splitting technique. For each step forward in time, there are three distinct substeps: 1) the Lagrange step, 2) the mesh relaxation step, and 3) the advection step. In the Lagrange step, the velocity of the reference frame is set equal to the fluid velocity and it is allowed to move with the fluid (Fig. 2). At the end of the Lagrange step, the mesh is moved to an arbitrary position to relieve the mesh distortion during the mesh relaxation step. The system is now frozen in time and the fluid variables at the new mesh positions are recalculated by means of an advection calculation. At the end of the advection step, the time step for the next iteration is calculated and the solution proceeds to the next time step.

A finite element method is used to discretize the equations. Spatial discretization is accomplished by a mesh of linear hexahedral elements. Physical quantities are assigned to staggered locations in the finite element. Velocities and accelerations are stored at the element nodes and vary trilinearly over the element. The element pressure, energy, and q term are stored at the element center and are constant over the element. Mass is stored at both the element center and element nodes, with the nodal mass being one-eighth the sum of the surrounding element masses.

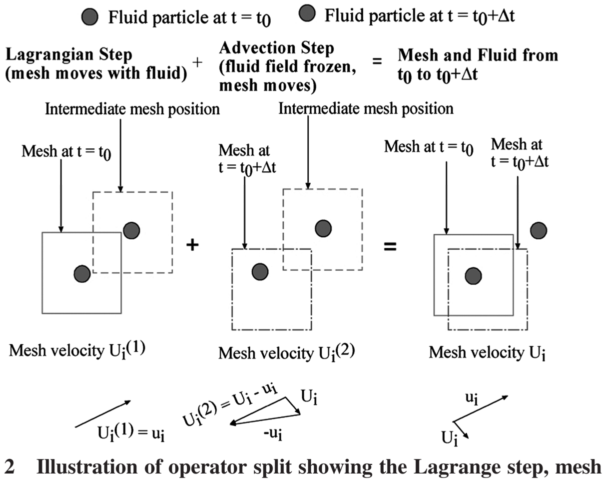

Fig. 2 Illustration of operator split showing the Lagrange step, mesh motion, and advection.

For temporal discretization, the velocities and the q terms are calculated at half-times, denoted by the superscript $n \pm \frac{1}{2}$, with all other quantities evaluated at full times. This staggering of dependent variables is a compact way of achieving equations that are centered in space and time and are thus second-order accurate [12].

A. Lagrange Step

In the Lagrange step, the mesh moves with the material. The convective terms in the governing equations thus drop out and the time derivative is recognized as the material derivative. The nodal accelerations are calculated from the discretized momentum equation, that is, Newton's second law $\mathbf{a} = \mathbf{F}/m$, where m is the nodal mass and $\mathbf{F}$ represents the total force on the node including pressure or shear stress, and any body forces due to rotation.

After calculating the nodal acceleration, centered differences are used to find the velocity at time $n + \frac{1}{2}$ and the new position of the node at time level $n + 1$. In general, the time step is allowed to vary during the simulation. However, with multiple blade rows, the time step is fixed to avoid interpolation in time when information is passed between the blade rows. This time step Δt is chosen small enough to satisfy the restrictions arising from the Lagrange and advection steps in all domains. Once the updated velocity and displacement fields are known, the deviatoric stress tensor can be obtained using the appropriate constitutive equation. For the case of the structure, the stress depends on the incremental displacement from the unstressed position, whereas, for the fluid, the stress depends on the instantaneous velocity gradients. Therefore, the stress tensor is updated for the structure but calculated at each time step for the fluid. The Lagrange step is completed using conservation of energy to update the elemental energy. For the solid, the energy equation is integrated using central differencing in time, whereas a third-order Runge–Kutta method is used for the fluid. At the end of the integration, the thermodynamic pressure of the fluid and mechanical pressure of the solid are updated using appropriate equations of state.

B. Turbulence Modeling

The Baldwin–Lomax [13] turbulence model is used to calculate the eddy viscosity in TAM-ALE3D. Although more advanced turbulence models exist, the Baldwin–Lomax model was chosen for computational efficiency and ease of implementation. In addition, it can be "tuned" relatively easily to many flows of interest. A relatively standard version of the Baldwin–Lomax model with a few modifications (similar to the ADPAC code [14]) is implemented in TAM-ALE3D [10]. The Baldwin–Lomax model is a two-layer model with separate equations for the eddy viscosity in the inner and outer layers and a smooth transition between the two different formulations. The eddy viscosity is given by

$$\mu_t = \begin{cases} (\mu_t)_{\text{inner}}, & y \leq y_{\text{crossover}} \\ (\mu_t)_{\text{outer}}, & y > y_{\text{crossover}} \end{cases} \tag{8}$$

where y is the normal distance to the nearest wall, and $y_{\text{crossover}}$ is the smallest y value at which the viscosities from the inner and outer formulations are equal.

The turbulence model is implemented in a manner capable of accommodating moving grids. Boundary-layer calculations are carried out in the wall normal direction and wake calculations across the entire wake. Inside the boundary layer, both the inner and outer formulations are used to determine the eddy viscosity, whereas only the outer formulation is used for wakes because there is no wall shear stress. To limit spuriously high values, the turbulent viscosity is limited to 1000 times the laminar value [15]. The turbulent viscosity thus calculated is added to the laminar viscosity to obtain the total viscosity used to calculate the shear stress from the Newtonian constitutive equation.

C. Mesh Relaxation

In the Lagrange calculation, the mesh moves with the continuum. Clearly, the fluid elements cannot continue to move in a Lagrangian fashion because element locking will occur due to large shear deformation. Therefore, before proceeding to the next time step, it is necessary to move the fluid mesh to a new position and recalculate the elemental and nodal quantities by an advection calculation. This process of moving the mesh to a new position is called mesh relaxation. The structural mesh is not relaxed because the solid can be modeled from a Lagrangian perspective throughout the simulation.

Successful prediction of wake-induced airfoil vibration requires that good mesh resolution be maintained in the airfoil boundary layer when the airfoil moves in response to the excitation. A mesh movement routine based on a spring analogy [16,17] is incorporated into the TAM-ALE3D solver to maintain boundary-layer mesh resolution for the duration of the forced response simulation. The mesh is replaced by an array of fictitious springs acting like an elastic medium. The equilibrium position of this mesh is taken to be the pre-Lagrange position, and any mesh motion during the Lagrange step is considered to be a distortion imposed on the mesh/spring system. By increasing the stiffness of the fictitious springs, better resolution can be attained close to the surface of the airfoil in the high-gradient regions of the flow.

D. Advection

As a fluid element moves from its position at the end of the Lagrange calculation to its new position after mesh relaxation, there is mass, momentum, and energy flux through the six faces of the element. The advection calculation is not performed for the solid because it can be modeled from a solely Lagrangian perspective.

Because advection is merely a geometric update of the mesh, the source terms on the right-hand side of the governing equations disappear. The new mass, momentum, and energy of the element are obtained by summing the flux of these quantities through the element faces using a second-order upwinding scheme. Monotonic limiters are used to ensure that these quantities are always bounded by the corresponding values in the upwind and downwind elements. Note that, because momentum is stored at the nodes, momentum advection is performed with a "node-centered" element.

E. Time Stepping

The maximum time step for this explicit calculation is calculated based on stability considerations using the Courant condition. Both the Lagrange and advection steps are considered when determining the maximum time step for the overall simulation, with this global time step being the smaller of the Lagrange and advection time-step sizes.

III. Boundary Conditions

A. Airfoil Surface Boundary

A no-slip boundary condition is required at the airfoil surface. In addition, momentum and energy must be exchanged between the airfoil and the flow at the interface. This is accomplished by requiring the fluid and airfoil nodes on this boundary to move as a single body during the Lagrange acceleration calculation. Interpolation routines allow for the fluid and airfoil nodes to be noncontiguous.

During the Lagrange or advection calculation, the fluid nodes can move away from the airfoil surface. Therefore, at the end of both these calculations, the fluid nodes on the airfoil are projected back onto the airfoil surface thereby maintaining geometric continuity at the airfoil surface. In addition, the velocities of these nodes are set to zero with respect to the airfoil. The fluid nodes at the blade trailing edge are allowed to move freely during the Lagrange calculation. However, after the advection calculation, their velocities are set to zero with respect to the airfoil.

B. Periodic Boundaries

Phase-lagged periodic boundary conditions of the form proposed by He [18] are used to transfer information between the periodic boundaries. These boundary conditions can be used to model the aerodynamics of isolated blade rows for an excitation with a nonzero interblade phase angle (IBPA). For problems involving multiple blade rows, the airfoil counts are scaled such that each blade row is represented by a few airfoil passages, with the periodicity condition on each blade row the same. For instance, in the case of a rotor/stator interaction simulation with a 19/18 blade/vane count, the number of stator vanes is increased to 19 so that only one blade passage need be analyzed for each domain, with the flow variables transferred directly between adjacent airfoil passage boundaries. This corresponds to a 360-deg IBPA.

C. Hub and Tip Boundaries

The cylindrical surfaces at the hub and tip are treated as slip surfaces, with the airfoils extending from hub to tip. Even though end-wall effects can be important, for the forced response effects considered here, the governing physics is essentially two-dimensional. Additionally, the coarse-grain parallelism in the solver means that the CPU time required to resolve the end-wall boundary layers would be significantly larger. Thus, the focus of the effort has been in advancing fluid–structure interaction capability more than secondary flow prediction capability.

To enforce the boundary condition, the fluid nodes next to the hub and tip surfaces are projected normally onto these surfaces, and the normal velocity component is set to zero at the end of both the Lagrange and advection steps. However, the airfoil nodes on the hub and tip are allowed to move and are not constrained to the hub/tip boundaries.

D. Inflow and Outflow Boundaries

For an axial subsonic flow, the velocity, density, and energy flux are specified at the inflow and static pressure at the outflow. During the Lagrange calculation, the specified exit static pressure is included in the force summation for those nodes on the outflow boundary. At the inflow, the velocities calculated from the nodal accelerations are ignored and overwritten by the specified inflow velocity. For the advection step, the fluxes at the inflow need to be specified. The density and energy flux are explicitly specified, and the momentum flux is calculated from the specified inflow velocity.

To minimize reflections at the inflow and outflow boundaries, boundary conditions of the type described by Giles [19] are used. These allow acoustic waves normal to the inflow and outflow boundaries to pass out of the domain without reflection.

The inflow boundary is made partially nonreflecting by adding the following perturbations to the specified inflow quantities:

$$\Delta\rho^{\text{inflow}} = -\frac{\rho_{\text{avg}}\Delta u_1^{\text{ext}}}{2A_{\text{avg}}} + \frac{\Delta P^{\text{ext}}}{2A_{\text{avg}}^2} \tag{9}$$

$$\Delta u_1^{\text{inflow}} = \frac{\Delta u_1^{\text{ext}}}{2} - \frac{\Delta P^{\text{ext}}}{2\rho_{\text{avg}}A_{\text{avg}}} \tag{10}$$

$$\Delta(\rho E)^{\text{inflow}} = \frac{1}{(\gamma-1)}\left[-\frac{\rho_{\text{avg}}A_{\text{avg}}\Delta u_1^{\text{ext}}}{2} + \frac{\Delta P^{\text{ext}}}{2}\right] \tag{11}$$

where the superscript "ext" indicates that this perturbation quantity is extrapolated from the interior, adjacent to the inflow boundary, the subscript "avg" denotes the time average, with this being the user-specified properties at inflow, and the velocity under consideration in this one-dimensional nonreflecting boundary condition being the velocity normal to the boundary.

The outflow boundary condition is slightly more involved. For the case of a diffuser-excited radial impeller, the unsteady aerodynamic response of the impeller to excitation from the downstream diffuser is modeled as an incoming acoustic wave at the outflow boundary. Therefore, at the outflow boundary, the specified time-averaged pressure is perturbed with

$$\Delta P^{\text{outflow}} = \tfrac{1}{2}(\rho_{\text{avg}}A_{\text{avg}}\Delta u_1^{\text{ext}} + \Delta P^{\text{ext}} + c_3) \tag{12}$$

where c_3 is the characteristic associated with the upstream going acoustic wave and given by

$$c_3 = \text{Im}[-\rho_{\text{avg}}A_{\text{avg}}\Delta u_1 + \bar{P}e^{i(m\eta+\omega t+\phi_0)}] \tag{13}$$

In Eq. (13), the incoming acoustic excitation waveform is assumed to be $\Delta P = \bar{P}\sin(m\eta + \omega t + \phi_0)$, with amplitude $\bar{P}$, tangential wave number m, and initial phase ϕ_0. The tangential coordinate is η, and Δu_1 is the velocity perturbation associated with the acoustic wave. For problems where there are no incoming acoustic waves at the outflow, the characteristic c_3 is zero.

IV. Multidomain Calculations

Parallel computations are performed by placing a segment from each blade row on a processor. Information passing between processors is accomplished with message passing interface standard library calls. For blade rows with equal blade counts, this segment is a single blade passage, with periodic boundaries accounting for the complete blade row. To simplify the interpolation between upstream and downstream domains, there are equal numbers of element faces on the interface between domains, equally spaced tangentially and radially.

In the Lagrange calculation, the nodal forces due to the element pressure, the q term, and the hourglass viscosity are first calculated without accounting for the presence of the other domain. These forces, as well as the nodal masses at the inflow boundary of the downstream domain, are then passed to the upstream domain. The two domains are offset due to rotation, so interpolation is performed and the forces and masses added to the upstream outflow boundary nodal forces and masses. The net nodal acceleration is calculated by dividing the net nodal force by the net nodal mass. These accelerations are passed to the downstream domain and interpolated to the downstream nodal locations. Finally, any Coriolis and centripetal accelerations are added.

For the advection of mass and energy, second-order accuracy is maintained at the interface between domains. The momentum advection calculation at the outflow boundary of the upstream domain is performed without information from the downstream domain, that is, the interface is treated as an outflow boundary. The computed velocities are then passed to the inflow boundary of the downstream domain. These velocities are interpolated to the downstream nodal positions and then transformed to account for the relative rotation between domains.

V. Results

TAM-ALE3D results are presented for the following turbomachinery aeromechanics problems, with comparisons to analytical results or experimental data where available: 1) analysis of crack generation in the IGVs in a transonic axial-flow compressor, 2) flow-induced vibratory response of stator vanes in a transonic axial-flow compressor, 3) diffuser-excited high-speed radial flow impeller aerodynamic response, and 4) aerodynamic damping at impeller exducer.

The geometry used for the axial compressor studies discussed here is the Purdue transonic compressor. The baseline configuration of the compressor features a one-and-a-half-stage axial-flow geometry representative of that used in the front stages of advanced aircraft engine high-pressure compressor designs. The compressor has a design speed of 20,000 rpm and a maximum pressure ratio of 1.38. The test section has a constant hub–tip ratio of 0.67 with a tip diameter of 0.3 m (12.0 in.) and features 18 IGVs, a rotor with 19 blades, and 18 downstream stator vanes. The rotor blades consist of NACA 65 series profiles on circular arc meanlines with a 5.08-cm (2.0 in.) chord and a thickness distribution varying from 10% at the root to 6% at the tip. The IGV and stator vanes are an advanced controlled diffusion airfoil design with a 4.45-cm (1.75 in.) chord and a constant 7% thickness.

For both axial compressor simulations, the vane counts are increased to 19 so that the vane/blade count is now 19/19 instead of 18/19. Thus, the blade row interaction (IGV–rotor or rotor–stator) can now be modeled using just one blade passage per blade row, with the interblade phase angle now 360 deg.

The geometry used for the radial flow impeller study is that of the Purdue High-Speed Centrifugal Compressor which consists of a titanium impeller, a radial-vaned diffuser, a discharge plenum, and a bearing housing to support the compressor shaft. The compressor has a nominal operating speed of 48,450 rpm, a maximum pressure ratio of 5.4, and a maximum mass flow rate of 5.5 lb_m/s (2.5 kg/s).

A. Analysis of Crack Generation in Inlet Guide Vanes in a Transonic Compressor

The primary unsteady aerodynamic forcing function for IGV vibrations is the potential field (at subsonic operation) or shock (at transonic operation) from the downstream rotor. The ability of TAM-ALE3D to predict these forcing functions and the resulting IGV unsteady aerodynamic response has been validated for both subsonic and transonic operation of the Purdue transonic compressor [20]. Figure 3 shows the rotor-generated forcing function and the resulting IGV aerodynamic response at the nominal part-speed operating condition of 15,000 rpm, with the inviscid simulation run to match the measured mass flow rate of 9.09 lb_m/s. These results were obtained with a mesh of 22,610 elements for the IGV passage and 24,852 elements for the rotor passage using the inviscid TAM-ALE3D aerodynamic model. Both passages feature 19 layers of elements in the spanwise direction.

The relative phase shift between the simulation and experiment is adjusted to give the best match between the results. The times at which to compare the TAM-ALE3D results to other experimental data are determined by referring to this forcing function result. The predicted forcing function is in very good agreement with the data. The experimental forcing function has higher frequency components that are not predicted by TAM-ALE3D. The miss in higher harmonics could be due to the absence of IGV wakes, which would cause a periodic incidence variation on the rotor and hence a modulation in the rotor potential field (forcing function to IGV). As far as the vane unsteady aerodynamic response is concerned, the trends predicted by TAM-ALE3D and exhibited by the data are similar, but TAM-ALE3D tends to predict larger unsteady pressure fluctuations over the whole IGV chord. However, the overall agreement between prediction and data is satisfactory.

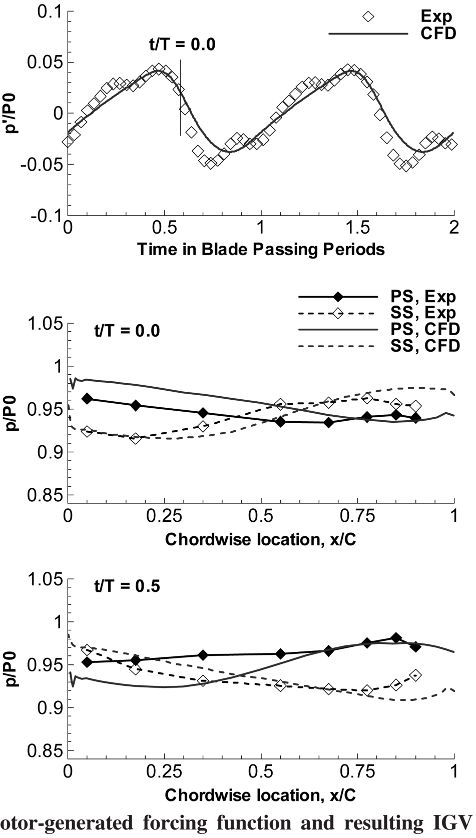

Fig. 3 Rotor-generated forcing function and resulting IGV aerodynamic response at 15,000 rpm.

During extended operation of the transonic compressor facility at 15,000 rpm, the IGVs cracked at four locations (Fig. 4). A trailing-edge flapping mode with a natural frequency of 4200 Hz (corresponding to a rotor rotational speed of 13,260 rpm) is responsible for the cracking.

Because the operating speed (15,000 rpm) is far removed from the rotor resonant speed of 13,260 rpm, the IGV failure at the 15,000 rpm operating condition was rather surprising. To investigate the reason for the unexpected failure of the vanes at 15,000 rpm, a TAM-ALE3D fluid–structure analysis was used [21].

Two part-speed rotor operating conditions are considered: 14,000 and 15,000 rpm, which correspond to excitation frequencies on the IGV of 4433 and 4750 Hz, respectively. Figure 5 shows a two-dimensional slice of the tip of the mesh used for both the IGV and rotor blade passages, with the IGV and rotor passage meshes consisting of 9680 and 9152 fluid elements, respectively, with 11 elements along the span. The aluminum IGV structural mesh consists of 2204 elements, with 4 elements across the vane thickness. The natural frequency of the IGV trailing-edge flapping mode determined using this mesh is 4024 Hz, which is within 5% of the experimentally determined value.

Figure 6 shows the time-variant von Mises stress for the four high-stress regions of Fig. 4. The stress at 15,000 rpm is nearly triple that at 14,000 rpm at the locations shown, even though the 14,000 rpm condition is closer to the resonant frequency of the mode. This unexpected result is explained by observing the magnitude of the modal forcing obtained by an aerodynamics-only calculation (Fig. 7). The modal forcing for the trailing-edge flapping mode increases by a factor of 4 as the speed increases from 14,000 to 15,000 rpm. This shows that the large modal forcing at the off-resonance condition is mainly responsible for the increased cyclic stresses and HCF failure of the IGVs, a fact which is consistent with the observed cracking [21].

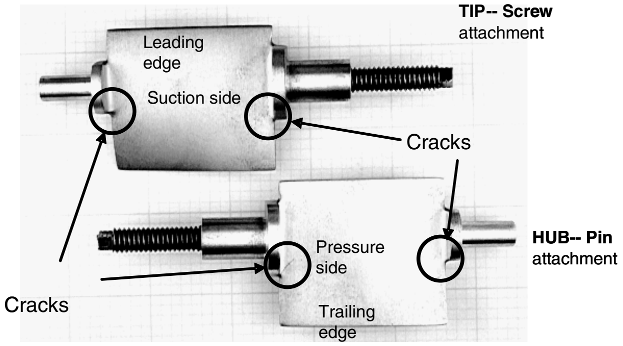

Fig. 4 HCF failure locations for the IGVs.

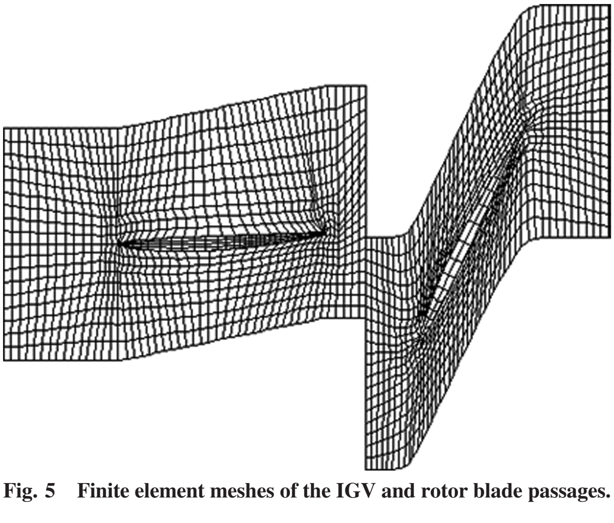

Fig. 5 Finite element meshes of the IGV and rotor blade passages.

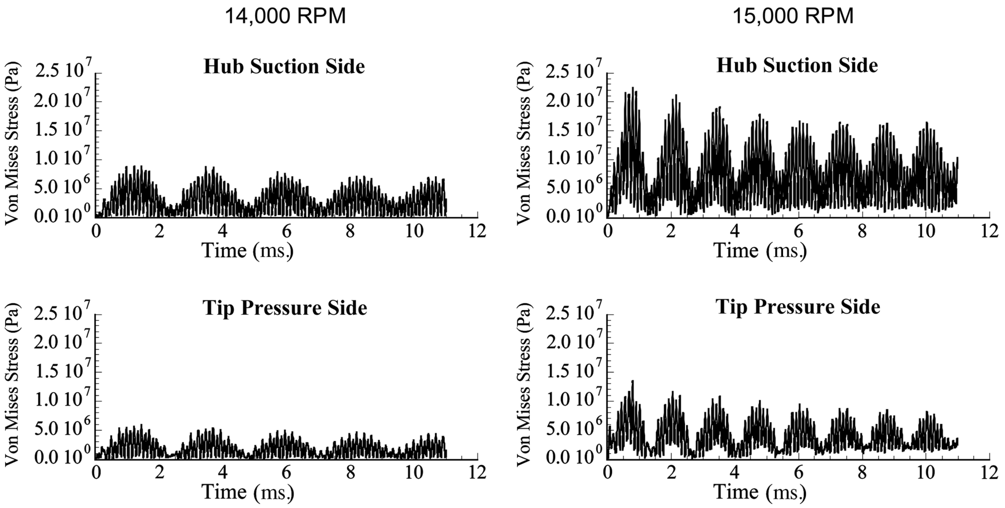

Fig. 6 IGV von Mises stress time histories.

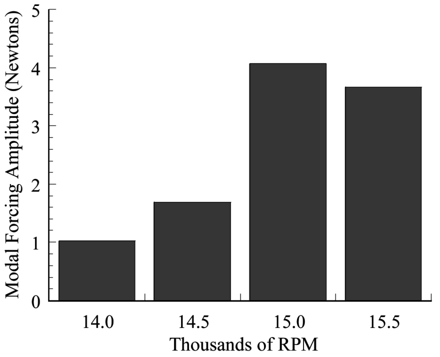

Fig. 7 Modal forcing amplitude versus rotor speed.

B. Flow-Induced Vibration of Stator Vanes in a Transonic Compressor

The original version of TAM-ALE3D employed in the IGV calculations [20,21] was restricted to Euler and laminar viscous calculations, and was therefore only able to address potential/shock forcing functions. However, turbulent airfoil wakes are the primary forcing function resulting in HCF. Thus, to predict the response of blade rows to wake forcing functions, TAM-ALE3D modeling capabilities were extended to model turbulent wakes by Ramakrishnan [10] by incorporating the Baldwin–Lomax turbulence model into the flow solver.

Experiments and modal analysis of the Purdue transonic compressor stator vanes indicate that the vane's third natural mode is excited by upstream rotor wakes near the part-speed operating point (15,000 rpm). To investigate this operating point, the viscous analysis was first experimentally validated by comparing the rotor–stator interaction aerodynamics with data. TAM-ALE3D modal predictions of the stator vane were then compared to data. Finally, a fluid–structure interaction analysis was used to simulate the resonant response of the stator vanes to unsteady aerodynamic excitation at the vane's third natural frequency [22].

For the aerodynamics-only calculation, the rotor passage is modeled with 37,770 hexahedral elements and the stator passage with 41,040 elements. The airfoils are modeled with shells and are held fixed during this simulation. The rotor passage uses a C grid wrapped around the blade surrounded by H grids in the wake and outer "inviscid" regions, with a total of 52 points in the axial direction and 49 points in the blade-to-blade direction. The stator passage is composed entirely of H grids, with 58 points axially and 49 points in the vane-to-vane direction. Both passages have 16 points in the spanwise direction and 16 points in the wall normal direction near the airfoils to resolve the boundary layers. In addition, the trailing edge of the rotor blade and the leading and trailing edges of the stators are modified into wedges. The smallest value of the near wall mesh spacing is about $y^+ = 1$ for the rotor and $y^+ = 0.2$ for the stator passage mesh. A grid resolution study is performed using a coarser grid with $(16 \times 29 \times 40)$ nodes in the radial, tangential, and axial directions for both the rotor and the stator. This grid has 50% fewer elements than the fine grid and only eight points in the boundary layer. It must be noted that the spanwise resolution is the same for both grids for this essentially two-dimensional problem of wake-induced forced response.

The simulation "operating point" is characterized by a total pressure ratio of 1.18 and a mass flow rate of 9.13 lb_m/s with the corresponding measured values being 1.18 and 9.09 lb_m/s, respectively. Figure 8 shows the stator vane surface predicted and measured instantaneous aerodynamic response at the times corresponding to the wake forcing function results shown in the

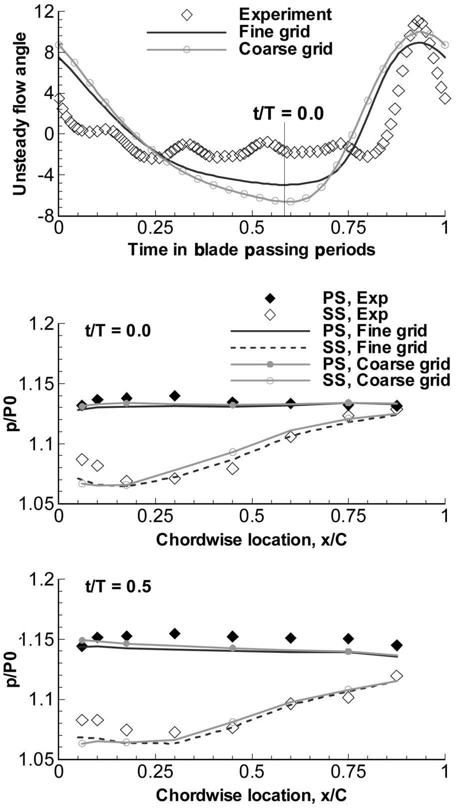

Fig. 8 Rotor wake-generated forcing function and resulting stator vane aerodynamic response.

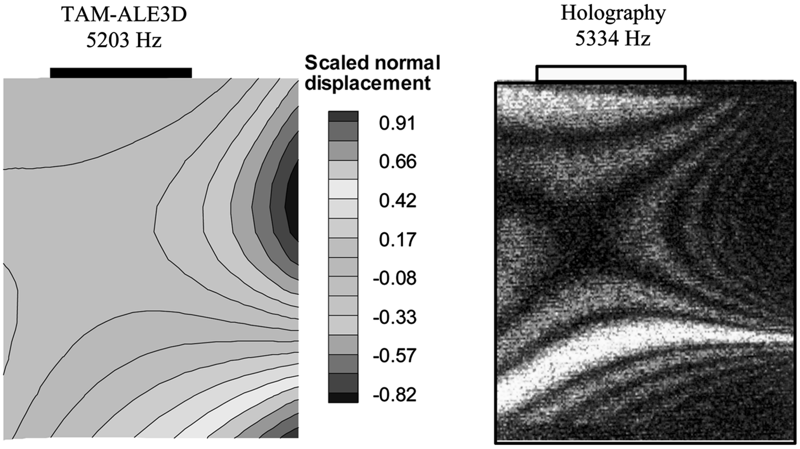

Fig. 9 Predicted and measured stator mode 3.

figure center. The forcing function is represented in terms of the absolute perturbation flow angle which is related to the stator incidence and is also a very sensitive indicator of the rotor wake characteristics. The simulation somewhat overpredicts the depth of the rotor wake and misses the higher harmonics in the data. However, the predicted instantaneous stator surface pressures exhibit very good correlation with data. The suction and pressure surface pressure fluctuations are approximately 180 deg out of phase [23], with this phase shift very prominent near the leading edge, as expected.

The structural dynamic capabilities of TAM-ALE3D are again validated by extracting the modal properties of the stator vane. Figure 9 shows the mode shape of the third mode obtained from a TAM-ALE3D impulse test of the stator vane in vacuum with comparison to holographic data. As seen, the TAM-ALE3D mode shape matches the measured holographic mode shape very well. The predicted natural frequency (5203 Hz) also agrees well with the measurement (5334 Hz), with the discrepancy being less than 5% for this vane mesh employing only 2464 elements.

A fluid–structure interaction analysis of the rotor–stator interaction at the rotational speed corresponding to the stator vane's third natural frequency was then performed to quantify the stator vane vibratory response. Figure 10 shows a midspan slice of the rotor and stator passages used for the simulation. The vane structural grid is the same as that used to determine the natural frequencies and mode shape. The rotor blade is also modeled with hexahedral elements but its response is not of interest. Therefore, it is fixed throughout the duration of the simulation. The rotor and stator passages are modeled with approximately 27,000 and 28,000 elements, respectively, with 15 elements each in the spanwise direction. The topology of these fluid–structure meshes is the same as the aerodynamic meshes described earlier.

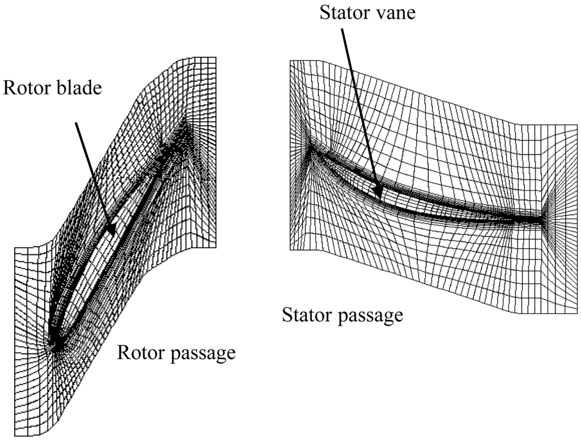

Fig. 10 Midspan rotor and stator passage meshes for fluid–structure interaction.

Figure 11 shows the time history of stress intensity amplitudes at three different locations on the vane denoted by "ssfx," "psfx_te" (corresponding to nodes that are fixed, i.e., on the interface between the trunnion and the vane), and "pste," a free node just outside the trunnion/blade interface.

The predicted maximum stress intensity level is approximately 8.5 ksi (58.6 MPa). A frequency spectrum shows that the contribution from the resonant frequency is approximately 3 ksi (20.7 MPa), with the rest of the stress coming from lower frequency modes that eventually decay with time.

There are no stator vane stress data available for a direct comparison. But, stress data are available on the reconfigured Purdue transonic compressor rotor blisk excited by upstream IGV wakes [24]. The mean resonant stress at the nominal loading condition for the second bending mode with a mean resonant frequency of 5693 Hz (corresponding to a rotor speed of 17,079 rpm) was 5.34 ksi (36.8 MPa).

In the context of the current problem, stator vanes typically have significantly larger mechanical damping than rotor blisks. Additionally, the excitation from the wakes is expected to be quite weak for the thin wakes encountered at operation close to the design point of the subsonic NACA 65 rotor. Therefore, the predicted stator vane resonant stress value of 3 ksi (20.7 MPa) is in the vibratory stress range expected for wake-induced forced vibration of a stator vane.

C. Diffuser-Excited High-Speed Centrifugal Impeller Aerodynamic Response

The vaned diffuser potential field and/or shock structure is a significant source of excitation to the rotating impeller in high-speed centrifugal compressors. The impeller responds to the diffuser forcing function, with the tips of the inducer and impeller blades exhibiting flow-induced vibration and HCF.

Although the actual forcing function for the impeller is the spatially nonuniform, unsteady potential field/shock structure at the entry to the vaned diffuser, this "forcing function" is the result of the unsteady aerodynamic interaction between the impeller and diffuser. Modeling the resulting impeller unsteady aerodynamic response entails simulation of unsteady impeller–diffuser interactions, requiring extensive computational resources.

To simplify the problem, the impeller and diffuser are decoupled, with the primary part of the forcing function to the impeller now being the time-averaged, spatially nonuniform vaned diffuser potential field. In the first-order approximation here, the first harmonic of the measured [25] time-averaged diffuser potential field is used to represent the forcing function, with viscous effects ignored. Euler simulations of the impeller aerodynamics are used to study the behavior of the diffuser generated forcing function. The chosen harmonic of diffuser excitation to the impeller is modeled as a traveling pressure wave at the exit of the impeller computational domain, that is, the diffuser inlet, with phase-lagged periodic

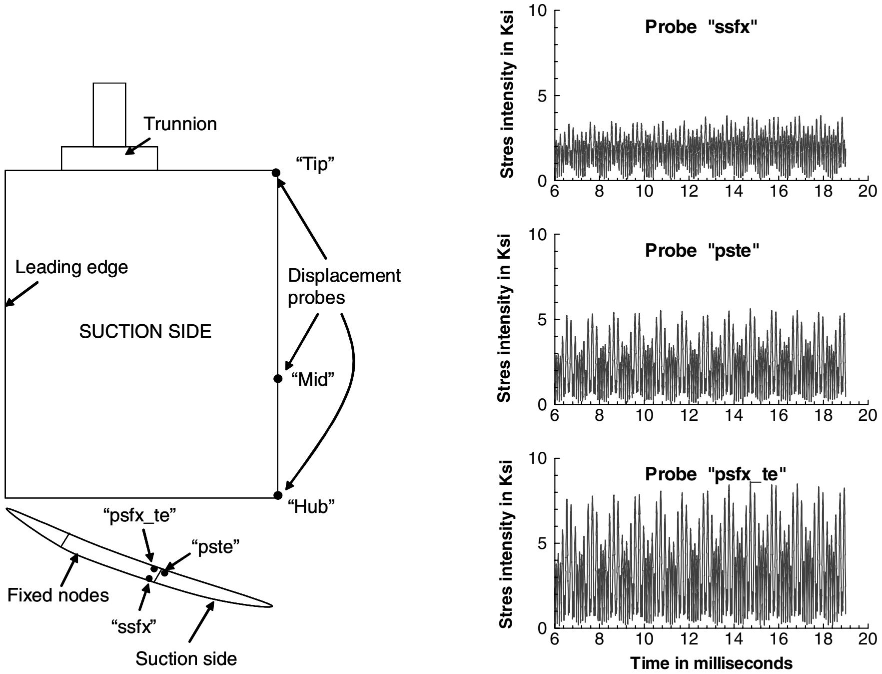

Fig. 11 Stator vane forced vibratory stress intensity amplitudes.

boundary conditions on the impeller accounting for the correct periodicity of the impeller–diffuser interaction.

1. Upstream Propagating Acoustic Waves

The diffuser excitation is modeled as a traveling pressure wave at the impeller exit in the rotating frame of reference. To perform these simulations, the outflow boundary condition was modified by Ramakrishnan [11] to allow upstream propagating acoustic waves into the computational domain. Figure 12 shows the predicted unsteady loading due to upstream propagating acoustic waves on a radial cascade at a large value of mean radius. The loading predictions compare well with the analytical solver LINSUB, thus validating the ability of TAM-ALE3D to simulate similar unsteady loading of the impeller by the vaned diffuser potential field.

2. Impeller Unsteady Aerodynamics

The flow passage for the simulations consists of a primary blade and a splitter blade with the outflow boundary at the diffuser inlet. The inflow boundary is placed at the lowest radius of the spinner attached to the front of the impeller. Tip clearance and the impeller disk are not modeled. The computational domain for the flow passage therefore consists of approximately 99,000 elements with ($11 \times 39 \times 216$) elements in the spanwise, blade-to-blade, and meridional directions. The 216 elements in the meridional direction are inclusive of the 34 elements in the vaneless space. The vaneless space has 16 elements in the tangential direction to resolve the expected regions of low velocity flow behind the blade trailing edges, in addition to the 39 passage elements. Both blades and flowpath are modeled with hexahedral elements, although the blades are held fixed throughout the simulation. The flow mesh is especially fine in the exducer region and the vaneless space where the propagation of the high-frequency acoustic waves of the diffuser forcing function is of interest. A slightly coarser mesh employed for the exducer damping calculation is shown in Fig. 13. The mesh is very coarsely spaced upstream of the inducer, similar to the approach used by Rangwalla and Rai [26] to numerically dissipate reflections from the inflow boundary.

The operating line considered in this study is the 90% speed line of the Purdue high-speed centrifugal compressor measured by Gallier [27]. However, using the inviscid impeller model, it is not possible to exactly match the flow turning and losses characteristic of the actual machine at any operating point. Additionally, because of the steepness of the inviscid "machine" characteristic, the solution is very sensitive to the exit pressure imposed. A slightly higher exit pressure can cause reverse flow, whereas a lower one can produce choked flow with very high Mach numbers [28]. However, varying the exit pressure did not produce any significant shift toward the measured operating line in this case. Therefore, the wheel speed is reduced to bring the pressure ratio and mass flow rate closer to the measured point, with three different wheel speeds: 75, 80, and 85% tested. The 80% speed tests produced converged results that are used in this study.

Figure 14 shows results from the aerodynamics-only simulation with the steady solution shown in the center. The diffuser pressure field first "impacts" the pressure side of the impeller main blade and

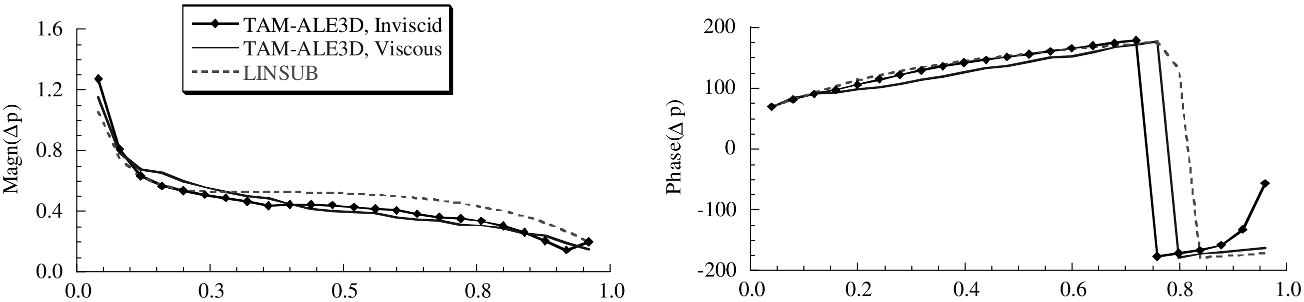

Fig. 12 Amplitude and phase of unsteady loading over a radial flow flat plate cascade at zero stagger.

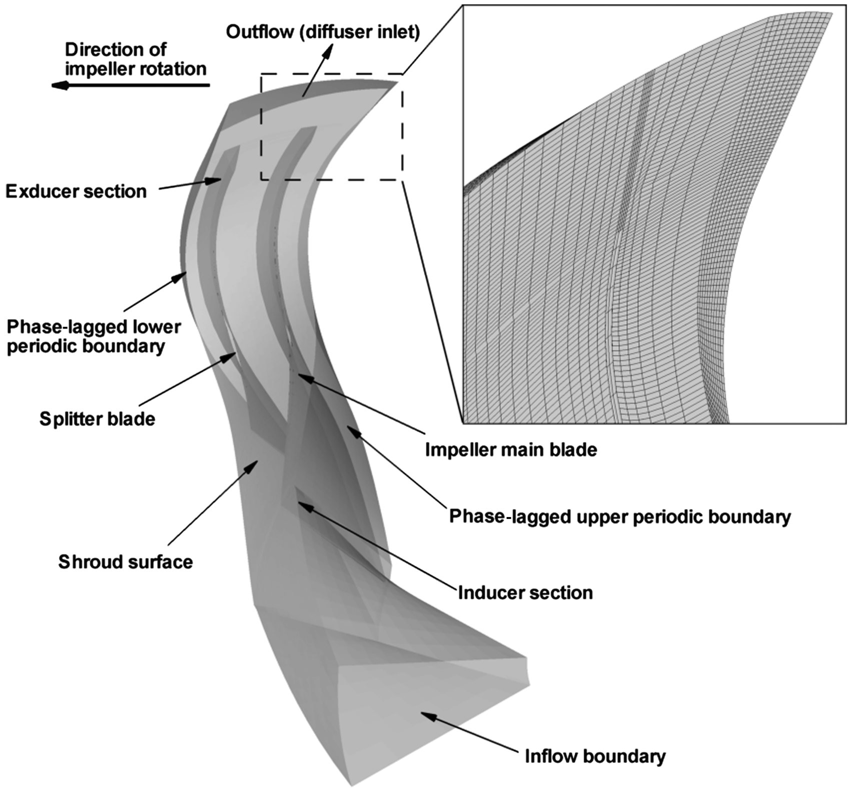

Fig. 13 Purdue High-Speed Centrifugal Compressor flow geometry and mesh.

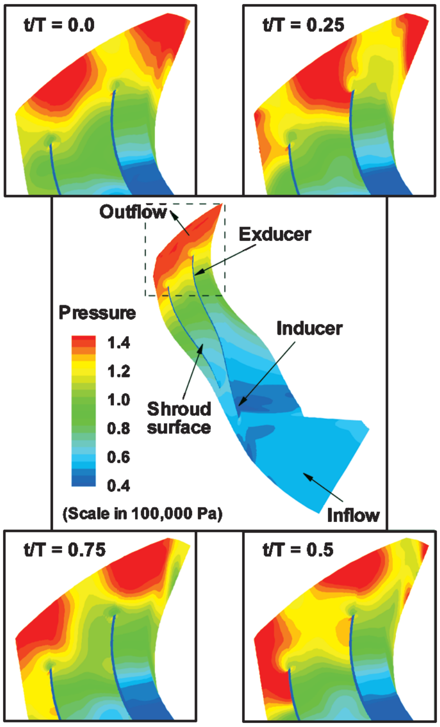

Fig. 14 Impeller passage pressure contours at four equally spaced instants in a vane pass cycle.

diffracts around the trailing edge to reach the suction surface. It then travels a short distance down the impeller passage on the pressure side of the blade before decaying. A similar phenomenon is observed on the pressure side of the splitter blade as well, starting with the next lobe of the diffuser pressure field, with the wave propagating farther along the splitter than the main blade. For both blades, most unsteadiness is observed on the pressure side, with the unsteadiness confined to the radial portion of the flow passage. Similar observations were also reported in the impeller–diffuser interaction studies of Domercq and Thomas [29] and Smythe et al. [30], both of which showed that the diffuser influenced only the exit portion of the impeller and that the unsteadiness was present primarily on the blade pressure surfaces. The excitation from the diffuser is thus confined to the radial portion of the blade for this case.

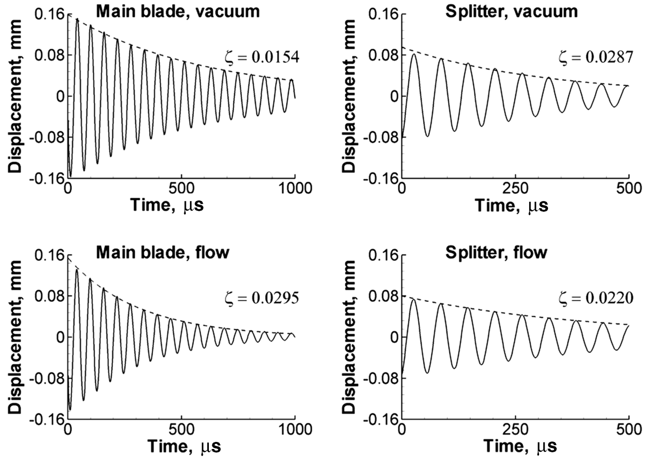

Fig. 15 Damping of blade trailing-edge motion in vacuum and in flow.

Table 1 Damping ratios for blade vibratory response

Damping source	Main blade	Splitter
Nonaerodynamic	0.0154	0.0287
Total	0.0295	0.0220
Aerodynamic	0.0141	−0.0067

Table 2 CPU time taken for fluid–structure interaction calculations

Case (machine)	Total number of elements	Time steps/period	CPU s/time step/10,000 elements
IGV forced response (SGI RS 10,000)	11,884	13,241	0.94
Stator vane forced response (IBM SP2)	30,664	12,813	0.65
Impeller blade aerodynamic damping (IBM p690)	66,728	4587	0.41

D. Exducer Aerodynamic Damping

The aerodynamic damping at the exducer is now evaluated by means of a fluid–structure interaction calculation. Figure 13 shows the fluid–structure mesh employed for the calculation, with the blade mesh consisting of 1960 elements and the total number of elements in the domain being 66,728. The flow passage mesh features ($11 \times 26 \times 216$) elements in the spanwise, blade-to-blade, and meridional directions.

The impeller main and splitter blade exducers are first impulsed in vacuum by a harmonic excitation at the natural frequency of the impeller main blade. Note that the harmonic excitation arises from an applied nodal force and not the diffuser vane potential field. After a periodic steady state of vibration is reached, the excitation is switched off to allow the vibration to decay slowly, with this decay caused by the hourglass and artificial viscosities in the TAM-ALE3D finite element model. (Hourglass viscosity [6] is the damping that is used to resist the growth of hourglass or zero energy modes of deformation in the structure.) The test is repeated in a flowfield devoid of diffuser excitation (i.e., periodic flowfield), with the difference in decay rates caused by the aerodynamic damping. Figure 15 shows the vibration decay for both main and splitter blades, with the aerodynamic damping at the exducer tabulated in Table 1. This procedure of extracting the aerodynamic damping has been used previously by Gottfried and Fleeter [31].

Although the difference in nonaerodynamic damping between the splitter and main blade can be understood on the basis of the fact that the splitter is a stiffer blade, the large difference in the aerodynamic damping values is very surprising. This suggests that the mean flow may play an important role in the vibration behavior because the mean flowfield around the splitter is different from the main blade due to the absence of an inducer.

E. CPU Time Considerations

An important area of concern in applying TAM-ALE3D to larger problems has been the long run times entailed per simulation. In fact, all simulations in this paper employed the coarsest grids possible to simulate the unsteady interaction while minimizing the run time. Table 2 lists the CPU times taken for the fluid–structure interaction calculations presented here in terms of the number of CPU seconds consumed per time step per 10,000 elements in the calculation. Note that all simulations used only one processor per blade row, that is, two processors each for the IGV–rotor and rotor–stator interaction calculations, and one processor for the impeller blade aerodynamic damping simulation. From Table 2, the reduction in the consumed CPU time due to increased computer capacity is obvious.

Although computer capabilities are increasing, the time required for a fluid–structure calculation using industry-standard grids is still unacceptably large using TAM-ALE3D. For example, a calculation using 4 million elements per blade passage/row would consume 210 hrs/period of oscillation if 4587 time steps per period are employed on a single processor. However, this unacceptably large run time can be greatly improved by better parallel processing in place of the coarse-grain parallelism currently in use, or by employing more efficient time-stepping schemes, or a combination of the two. For instance, using 32 processors on the IBM p690 and assuming only a 20x speedup implies 10–11 hrs/period of oscillation for this 4 million element mesh, which is within the realm of today's unsteady calculations.

VI. Conclusions

The development and application of the coupled fluid–structure interaction solver TAM-ALE3D has been described. The incorporation of turbomachinery-specific algorithms into TAM-ALE3D resulted in predictions of IGV vibratory failure in a modern transonic compressor. The addition of the next level of modeling capability, namely the ability to model turbulent wake forcing functions, enabled TAM-ALE3D predictions of stator vane vibratory stresses.

The addition of outflow boundary conditions to model incoming acoustic waves has enabled TAM-ALE3D to simulate high-speed impeller unsteady aerodynamic response to vaned diffuser excitation. The results show that the unsteadiness on the impeller blade is primarily confined to the pressure side of the exducer, an observation also reported by other investigators. Calculation of aerodynamic damping at the exducer shows large variation between the main and splitter blades.

Although further enhancements in modeling capabilities such as inclusion of end-wall boundary layers, tip clearance, and phase-lagged blade row interaction are required for TAM-ALE3D, the results show promise in the ability of a coupled fluid–structure solver to simulate aeroelastic phenomena in turbomachines. The results make a case that, with increasing computer resources, a fully coupled fluid–structure interaction approach can become the method of choice for HCF design.

Acknowledgments

This research was sponsored in part by the U.S. Air Force Office of Scientific Research. This support is most gratefully acknowledged. Computational support for the simulations was provided in part by the Rosen Center for Advanced Computing at Purdue University and in part by the National Center for Supercomputing Applications grant number MSS050007N using the IBM p690. The first author thanks Venke Sankaran for discussions on time-stepping schemes for multiphysics problems.

References

[1] Sayma, A. I., Vahdati, M., and Imregun, M., "Multi-Bladerow Fan Forced Response Predictions Using an Integrated Three-Dimensional Time-Domain Aeroelasticity Model," *Proceedings of the Institution of Mechanical Engineers, Part C: Journal of Mechanical Engineering Science*, Vol. 214, Pt. C, No. 12, 2000, pp. 1467–1483. doi:10.1243/0954406001523425

[2] Sayma, A. I., Vahdati, M., and Imregun, M., "An Integrated Nonlinear Approach for Turbomachinery Forced Response Prediction, Part I: Formulation," *Journal of Fluids and Structures*, Vol. 14, No. 1, 2000, pp. 87–101. doi:10.1006/jfls.1999.0253

[3] Bakhle, M. A., Srivastava, R., Keith, T. G., Jr., and Stefko, G. L., "A 3D Euler/Navier-Stokes Aeroelastic Code for Propulsion Applications," AIAA Paper 97-2749, 1997.

[4] Smith, M. J., Hodges, D. H., and Cesnik, C. E. S., "Evaluation of Computational Algorithms Suitable for Fluid-Structure Interactions," *Journal of Aircraft*, Vol. 37, No. 2, 2000, pp. 282–294. doi:10.2514/2.2592

[5] Hirt, C. W., Amsden, A. A., and Cook, J. L., "An Arbitrary Lagrangian-Eulerian Computing Method for All Flow Speeds," *Journal of Computational Physics*, Vol. 14, No. 3, 1974, pp. 227–253. doi:10.1016/0021-9991(74)90051-5

[6] Benson, D. J., "Computational Methods in Lagrangian and Eulerian Hydrocodes," *Computer Methods in Applied Mechanics and Engineering*, Vol. 99, Nos. 2–3 1992, pp. 235–394. doi:10.1016/0045-7825(92)90042-I

[7] Donea, J., "Arbitrary Lagrangian-Eulerian Finite Element Methods," *Computational Methods for Transient Analysis*, edited by T. Belytschko, and T. J. R. Hughes, North-Holland, Amsterdam, 1983, pp. 473–516.

[8] Bendikson, O. O., "A New Approach to Computational Aeroelasticity," AIAA Paper 91-0939, April 1991.

[9] Gottfried, Dana A., "Simulation of Fluid-Structure Interaction in Turbomachines," Ph.D. Dissertation, Purdue Univ., West Lafayette, IN, 2000.

[10] Ramakrishnan, K., "Simulation of Unsteady Viscous Blade Row Interaction in Turbomachines Using the TAM-ALE3D Code," M.S. Thesis, Purdue Univ., West Lafayette, IN, 2001.

[11] Ramakrishnan, K., "Computational Investigations of Axial and Radial Flow Compressor Aeromechanics," Ph.D. Dissertation, Purdue Univ., West Lafayette, IN, 2005.

[12] Noh, W. F., "Numerical Methods in Hydrodynamic Calculations," Lawrence Livermore Lab., UCRL-52112, June 1976, pp. 52, 58.

[13] Baldwin, B. S., and Lomax, H., "Thin Layer Approximation and Algebraic Model for Separated Turbulent Flows," AIAA Paper No. 78-257, Jan. 1978.

[14] Hall, E. J., and Delaney, R. A., "Investigation of Advanced Counterrotation Blade Configuration Concepts for High Speed Turboprop Systems: Task VII-ADPAC User's Manual," NASA CR-195472, 1995.

[15] Turner, M. G., and Jennions, I. K., "An Investigation of Turbulence Modeling in Transonic Fans Including a Novel Implementation of an Implicit k-ε Turbulence Model," *Journal of Turbomachinery*, Vol. 115, No. 2, 1993, pp. 249–260.
doi:10.1115/1.2929231

[16] Batina, J. T., "Unsteady Euler Airfoil Solutions Using Unstructured Dynamic Meshes," *AIAA Journal*, Vol. 28, No. 8, 1990, pp. 1381–1388.
doi:10.2514/3.25229

[17] Blom, F., and Leyland, P., "Analysis of Fluid-Structure Interaction on Moving Airfoils by Means of an Improved ALE Method," AIAA Paper 97-1770, 1997.

[18] He, L., "An Euler Solution for Unsteady Flows Around Oscillating Blades," *Journal of Turbomachinery*, Vol. 112, No. 4 1990, pp. 714–722.
doi:10.1115/1.2927714

[19] Giles, M. B., "Nonreflecting Boundary Conditions for Euler Equation Calculations," *AIAA Journal*, Vol. 28, No. 12, 1990, pp. 2050–2058.
doi:10.2514/3.10521

[20] Gottfried, D. A., and Fleeter, S., "Turbomachine Blade Row Interaction Predictions with a Three-Dimensional Finite Element Method," *Journal of Propulsion and Power*, Vol. 18, No. 5, 2002, pp. 978–989.
doi:10.2514/2.6044

[21] Gottfried, D. A., and Fleeter, S., "A New Approach to Turbomachine Blading Cyclic Stress Prediction," *5th National Turbine Engine High Cycle Fatigue Conference*, March 2000.

[22] Ramakrishnan, K., Lawless, P. B., and Fleeter, S., "Finite Element Simulation of Turbomachine Blade Row Viscous Interactions: Vane Vibratory Stress Prediction," *Journal of Propulsion and Power*, Vol. 23, No. 1, 2007, pp. 212–220.
doi:10.2514/1.17187

[23] Sanders, A. J., and Fleeter, S., "Multi-Blade Row Interactions in a Transonic Axial Compressor, Part II: Rotor Wake Forcing Function and Stator Unsteady Aerodynamic Response," American Society of Mechanical Engineers Paper 2001-GT-0269, July 2001.

[24] Fulayter, R. D., "An Experimental Investigation of Resonant Response of Mistuned Fan and Compressor Rotors Utilizing NSMS," Ph.D. Dissertation, Purdue Univ., West Lafayette, IN, 2004.

[25] Carnell, W. F., Jr., "Aerodynamic Performance and Forcing Function Measurements in a High-Speed Centrifugal Compressor," M.S. Thesis, Purdue Univ., West Lafayette, IN, 2001.

[26] Rangwalla, A. A., and Rai, M. M., "A Numerical Analysis of Tonal Acoustics in Rotor-Stator Interactions," *Journal of Fluids and Structures*, Vol. 7, No. 6 1993, pp. 611–637.
doi:10.1006/jfls.1993.1037

[27] Gallier, K., "Experimental Characterization of High Speed Centrifugal Compressor Aerodynamic Forcing Functions," Ph.D. Dissertation, Purdue Univ., West Lafayette, IN, 2005.

[28] Denton, J. D., "Solution of the Euler Equations for Turbomachinery Flows, Part II: Three-Dimensional Flows," *Thermodynamics and Fluid Mechanics of Turbomachinery*, Vol. 1, edited by A. S. Ucer, P. Stow, and C. Hirsch, Martinus–Nijhoff, Dordrecht, The Netherlands, 1985.

[29] Domercq, O., and Thomas, R., "Unsteady Flow Investigation in a Transonic Centrifugal Compressor Stage," AIAA Paper 97-2877, 1997.

[30] Smythe, C., Liu, J., and Tan, C. S., "Forced Response Predictions in Modern Centrifugal Compressor Design," *10th National Turbine Engine High Cycle Fatigue Conference*, 2005.

[31] Gottfried, D. A., and Fleeter, S., "Aerodynamic Damping Predictions for Turbomachine Blade Rows Using a Three-Dimensional Time Marching Simulation," AIAA Paper 99-2810, June 1999.

F. Liu
Associate Editor